MAN/HEP/91/05

Pulse Simulation and The Longitudinal Coordinate in the OPAL Muon Barrel Chambers

G.A.Bahan

Department of Physics, University of Manchester, M13 9PL, U.K.

March 1991

Abstract. A study was made of the formation of pulse signals on the anode wire of an OPAL muon drift chamber. The solutions of the differential equations of an equivalent circuit to the chamber arrangement were used to generate wire signals. Modifications to these solutions were investigated and introduced into the analysis to provide a computer simulation of pulse signals from both ends of the wire for a known longitudinal (z) coordinate.

1 Introduction

The muon barrel detector is the direct product of Manchester's involvement in OPAL. It consists of 110 chambers, each containing 2 drift cells. Each cell is 60 *cm* wide (allowing a maximum drift distance of 30 *cm*) , up to 10.4 *m* long and 15 *mm* in depth. An anode wire centrally supported at 1.4 *m* intervals passes along the length of each drift cell. The wire is 50 μm diameter gold-plated tungsten and carries a tension of 1 N [1], [2]

Glass fibre board forms the top and bottom planes of the chambers. The outside of this board is copper coated and earthed to form a screen, and electrodes printed on the inside create the drift field. These electrodes are kept at positive potentials steadily increasing to 4.0 kV near the wire, which itself is at the even higher positive potential of 5.85 kV. Consequently although the signals have to be decoupled from DC, this arrangement means,

1. the need for an extra layer of insulation is eliminated since the aluminium supports and copper screen are grounded.
2. the positive ions formed by ionization are initially attracted to the glass fibre board between the cathodes since this is 'more negative' than the cathodes, until eventually a smooth drift field is formed.

The process of decoupling from DC results in the modification of the shapes of signals from the chamber, a discussion of this effect forms part of this paper. The central and next to central drift electrodes of each cell are divided longitudinally by periodic patterns, to form the so called *diamond* cathode pads [3]. The elaborate diamond pad system is only effective in determining the longitudinal, or z coordinate accurate to $\sim$ 1.5 *mm* providing a coarse z value is known, to indicate within which long diamond pad avalanching occurred.

Measurement of z is usually obtained through either "charge division" or timing methods. The method most suitable is dependant on the wire resistance and on the impedance of the amplifiers used to readout the signals.

A flow of charge along the two paths to the ends of the anode wire is expected subsequent to the formation of an avalanche. If the flow down the wire is viewed as a transmission line problem, each of the two pulses is the same initially. When they arrive at their respective ends they are identical in charge; dispersion along the wire affects the shape of the current pulses, making them longer and lower, but with the same area. If the amplifier impedances are perfectly matched so that the pulses are then absorbed, then the two charges have the same value, and contain no useful information about z. To obtain a "charge division" measurement the amplifiers must be mismatched, usually by giving them low input impedances. The signal obtained is then the sum of repeated reflections travelling to and fro along the wire, and in this case the sum at each end is inversely proportional to the wire resistance (and therefore the wire length) from the original pulse to the relevant amplifier[4].

These chambers cannot use conventional charge divisions, as a low impedance mismatching was unfortunately not possible. The cathode pad network must be correctly terminated to avoid unwanted reflections from one pad to the others [5]. This dictates the termination seen by the wire, and it is moderately matched to the characteristic impedance of the wire itself. To obtain the best measurement of z from the signals at the two ends one should combine information from the difference of arrival times with information from the sizes of the pulses, these differences in pulse size being due not to 'charge division' as discussed above, but to dispersion and other effects on the pulse shape. To investigate this we have taken a model of the chamber as an equivalent RC circuit, and simulated the effects of this circuit, and also of the readout electronics..

2 Acquisition of Test Pulses

2.1 The chamber arrangement

Chambers were set up in Manchester to observe the pulses generated by cosmic rays, 75 % of which are penetrating muons at sea level [6]. A gas mixture of argon (90 %) and ethane (10 %) just above atmospheric pressure was used in the chambers, identical to that used at the OPAL site. The argon provides the necessary avalanching at low field strengths, while the ethane is present for quenching.

Scintillators (of width ~ 1 *cm*) above and below the chambers were used to externally trigger an oscilloscope on which the pulses were observed, see figure 1. The scintillator positioning enabled various values of coarse z and angle of incident cosmic rays to be selected.

2.2 The pre-amplifier

Signals from the wire and pads initially enter the preamplifier, as shown in figures 2 and 3. Pre-amplifier boards are present at both ends of the chamber.

The 'clever' end houses board C, on which the amplification occurs and board D sits on the 'dumb' end of the chamber. Board D decouples dumb end signals from the high voltage DC and these signals are then passed onto board C for amplification. The difference in cable lengths between the boards is neglected in this analysis since the time constants involved are not significant as compared to those of other components.

The high voltage is introduced through sets of 33 MΩ resistors on board C. The parallel system is a precautionary measure: in case of failure on one side the other resistance still provides a path for the current. The diode across the high voltage supply ensures the anode wire is positive with respect to the cathode pads. Signals are decoupled from DC through ferrite transformers, which also introduce differentiation. The transformers operate with 6 turns producing a self inductance of around 1.65 x 10^{-5} H. The mutual inductance linkage between the coils is expected to be 80 $\sim$ 90 % in the frequency range appropriate to the chamber pulses ($\sim$ 5 MHz). The 2.2 nF capacitors enable the signal to flow while preventing DC passage between the wire and pads. The transistors provide a transfer from a current signal to a voltage across the video amplifier.

Probes on the preamplifier boards enabled the form of the signals at various stages of propagation to be observed on the oscilloscope.

3 Pulse Formation in the Chamber

The electromagnetic field of a high energy particle passing through the chamber will ionize the gas. This ***primary*** ionization produces clusters along the track. The primary electrons produce ***secondary*** multiplication according to a cluster size probability distribution. In this analysis, the ionization is assumed to be uniform, there is nothing to be gained here by adding random discontinuities but it should be remembered that slight irregularities in observed pulses could be accounted for by this clustering. For the argon/ethane mixture used the number of total ion pairs is expected to be ~ 90 *percm* [7] of which ~ 30 *percm* are primary (i.e. a secondary multiplication of around 3). Thus for a particle at normal incidence on the chamber around 140 electrons are likely to be generated along the track length, (though this number may be less if electrons produced in the non-uniform field near the chamber walls do not reach the anode). The ionizing particle may be regarded as crossing the chamber instantly, i.e. all primary and secondary electrons can be considered to be formed at the same time.

For simplicity, this report considers the OPAL chambers in the avalanche region as essentially a coaxial cylinder, with a central anode of 25 μm radius and surrounding cathode of 7.5 mm radius. The high field region close to the OPAL anode wire is essentially radial in compliance with this assumption. Since the electrons are created close to the anode, while the positive ions must drift across much larger distances, the typical electronic contribution to the signal is $< 1\%$ of the total [7]. Thus the time development of the signal may be deduced from the analysis of the ions alone.

For N positive ions formed at a distance x from the anode centre, *Sauli* [7], Eq. 35, gives the induced signal on the wire as,

$$V(t) = -\frac{QN}{4\pi\varepsilon_0 l}\ln\left(1+\frac{\mu^+ C V_0 t}{\pi\varepsilon_0 P x^2}\right) = -\frac{QN}{4\pi\varepsilon_0 l}\ln\left(1+\frac{a^2 t}{x^2 t_0}\right) \qquad (1)$$

where μ^+ is the mobility of the ions, 1.7 $cm^2 atm.s^{-1}V^{-1}$ in this case, C is the capacitance per unit length, and P the gas pressure in atmospheres. Adding contributions from equation (1) for ions starting at the anode surface, $x = a$, to ions formed at, $x = a + 4\lambda$, accounts for $\sim$ 95 % of the signal. Since the drift velocity of electrons in the chamber is 37 μmns^{-1} [1] and the mean free path is around 1 μm, then the positive ions arriving from the same avalanche were considered to be formed at the same instant, and the signals from equation (1) to start simultaneously. Avalanche multiplication of around 10^5 was taken as typical, that is to say 1 electron approaching the anode produces 10^5 due to avalanching, and the values of N determined accordingly. Different values of N merely modify the signal amplitude and not the shape and selecting a multiplication of $10^4 \sim 10^6$ would be equally useful in this analysis.

This assumes that the chamber length l is short, i.e. that the voltage at any instant is the same at all points on the anode. This shows the limitation of this formula. For a long chamber one could perhaps replace l by the longitudinal spread of the pulse but this only affects the overall size of the pulse.

3.1 Effect of drift lengths and angle of incidence on pulse shape

The signal induced from the avalanche of one electron must be summed for each of the $\sim$ 140 electrons that produce avalanching in order to find the induced signal for one ionizing particle incident on the chamber. There is a spread in arrival times for these electrons for several reasons.

As the electron cloud drifts through the gas it suffers from longitudinal diffusion. This may be significant at our largest drift distances, but at smaller distances it can be neglected. For simplicity we do not consider it here.

The primary and secondary electrons follow field lines of differing lengths to arrive at the anode. Figure 4 shows the pattern of field lines within the chamber, as calculated from a relaxation process . Electrons formed near the middle of a track follow shorter paths to the anode and begin avalanching before those formed at the edge of the chamber. A difference of approximately 60 ns exists between these two extreme cases and this will produce significant shape modification for our signals, for which the width is ~ 200 ns. (A further small variation arises as the different paths travel through regions where the electric field, and thus the velocity, is different, but we ignore this.) An additional complication is that muons penetrating the chamber at angles other than normal incidence produce electrons along the track, whose time of arrival at the anode contains an angular dependence, see figure 4.

To allow for these effects the chamber width was considered to be divided into 72 bins, each containing roughly 2 electrons produced by an incident muon. Differences in time of arrival at the anode, and hence time of avalanching, between electrons from different bins were then

calculated by a computer program. This program then combined the induced signal from a single avalanche for all primary and secondary electrons, with the appropriate avalanche start times. Thus, the time development of a pulse for a single detected particle, incident at angle ϕ was calculated, this voltage signal is referred to in future as $V_{tot.}(t)$.

4 Pulse Simulation

4.1 Circuit analysis from the chamber signal to the decoupling transformers

The form of the voltage signal $V_{tot.}(t)$ as calculated in the preceeding section was introduced into the circuit shown in figure 5 . This circuit is directly representative of the circuit from the chamber to the DC decoupled side of the transformers.

The drift chamber appears as a capacitor, the value of which was deduced by continuing the coaxial analysis and using the capacitance per unit length for a coaxial system. The voltage signal induced by the positive ion movements is inserted in series to this capacitance to form the part of the chamber common to both 'clever' and 'dumb' end signals. It is the resistive anode wire that determines the differences in signals between the two ends of the chamber, in figure 5 it is represented by the resistances WRC and WRD. A specific value of z coordinate for the avalanche may be selected by assigning WRC and WRD as appropriate, the sum of the two resistances must, however, always be 300 Ω, the total resistance of the anode wire. In reality, the wire acts together with the cathode pads to form a transmission line, so the wire could be regarded as a combination of resistors, capacitors and inductors. However, initial work suggests the time constants involved are such that the purely resistive approach is sufficiently accurate. The agreement of the simulation and real data, as will be subsequently demonstrated, validates this assumption

The complicated arrangements of resistances that appear on the preamplifier boards, figures 2 and 3 terminating the pads, are equivalent to a single 300 Ω resistance on each board (this is required to prevent reflections). Thus, they are replaced by the single resistances R_1 in figure 5.

The secondary circuits contain the inductance of the transformers and the resistances R_2 (50 Ω), this resistance corresponds to the terminating resistance at the cathode ray oscilloscope. Thus the output signals calculated from analysis of figure 5 correspond to the signals taken directly after the transformers when observed on an oscilloscope.

Since all the circuit parameters were known, then a pulse simulation could be achieved by obtaining solutions to the circuit equations of figure 5, equations (2) to (5),

$$L\frac{d^2I_1}{dt^2} + (R_1 + WRC)\frac{dI_1}{dt} + \frac{I_1}{C} + \frac{(I_1 + I_3)}{D} + M\frac{d^2I_2}{dt^2} = \frac{dV_{tot.}(t)}{dt} \tag{2}$$

$$L\frac{d^2I_3}{dt^2} + (R_1 + WRD)\frac{dI_3}{dt} + \frac{I_3}{C} + \frac{(I_1 + I_3)}{D} + M\frac{d^2I_4}{dt^2} = \frac{dV_{tot.}(t)}{dt} \tag{3}$$

$$L\frac{d^2I_2}{dt^2} + R_2\frac{dI_2}{dt} + M\frac{d^2I_1}{dt^2} = 0 \tag{4}$$

$$L\frac{d^2I_4}{dt^2} + R_2\frac{dI_4}{dt} + M\frac{d^2I_3}{dt^2} = 0 \tag{5}$$

The first derivatives of each current were substituted by a new variable to yield eight first order differential equations, and these were solved numerically using a program incorporating a NAG routine. D02BDF[8] was the NAG routine utilised, this uses a Runge-Kutta-Merson

method to perform the integrations, given suitable initial conditions, which were easily deduced from considering $V_{tot.}(t)$ at time $t = 0$.

4.2 The circuit from the transformers to the video amplifier

The high voltage anode clearly prevents direct observation of signals on the wire and therefore the closest point to the wire that signals can be taken for investigation is between points A and B on figure 2. Observations of pulses were made directly after the transformers, between points A and B, and at the MON C point of figure 2, using a LeCroy amplifier which provided a factor 10 amplification with negligible distortion. Under comparison, the shapes of the pulses at these points were found to be identical and thus the intervening circuitry assumed to have no shape modifying properties. The time constant of the 0.47 μF capacitor and 1 kΩ resistor on this part of the preamplifier board is large compared to the time scale of a typical pulse supporting this assumption. The transistor apparently provides amplification without observable distortion. Consequently, the nature of pulses at the MON C connection correspond to the pulses generated by the analysis given in the preceeding section.

4.3 Comparison of the pulses generated numerically to those observed

The circuit parameters of figure 5 were entered into the program together with the voltage generated by the positive ions $V_{tot.}(t)$. Values of WRC and WRD were chosen so as to simulate an avalanche close to the clever end. The solutions for pulses from both the clever and dumb end were stored against time in data files for $t = 0$ to $t = 1.5$ μs. Figure 6 shows the clever end signal solution in graphical form. The concentration of points on the solution is determined by the length of the integration steps taken by D02BDF, which are in turn dependent on the accuracy required. The accuracy remains roughly constant for each point and thus the integration length is required to be smaller at the rapidly varying parts of the curve.

The scintillators were arranged to trigger on events occurring at the clever end and figure 7 illustrates a black and white polaroid, at ISO 3000, of a typical pulse observed at MON C under this triggering. The comparison of observation and simulation is favourable. Both pulses display the same features on similar time scales, a sharp peak, of width $\sim$ 200 ns and negative undershoot lasting for well over 1 μs. The negative undershoot is anticipated as a result of the differentiating imposed upon the signal by the decoupling transformers.

Figure 8 shows the simulation over a range from $t = 0$ to $t = 0.5$ μs and figure 9 the corresponding pulse on a time base of 0.2 $\mu s div^{-1}$. This increased scale enhances a notable feature common to both simulation and observation, the secondary peak appearing to the right of the main peak at around half the amplitude. The simulation displays a kink suggesting a third peak attempting to appear. To investigate this the simulation was rerun with the mutual linkage of the transformers reduced to 60 %, see figure 10. This suggests that ringing effects are responsible for the formation of the kink.

As discussed in section 3.3 the angle of incidence of a detected particle affects the shape of the observed pulse. An angle of incidence of 45° was used in the simulation, figure 11, and the scintillators orientated to trigger on this angle, figure 12. The anticipated broadening for the positive part of the pulse is visible in both cases.

Figures 13 and 14 display the simulation and observation respectively, for a particle incident on the clever end as seen by the dumb end. Due to charge division the amplitudes of the signals are decreased as expected.

A favourable comparison between analysis and observation can be seen in the above cases, validating earlier assumptions and suggesting that the simulation provides a good description

of the chambers action.

5 Effect of the Video Amplifier, Shaper and Digitizer

5.1 The video amplifier

The signals on the pre-amplifier board are then modified by an amplifier which acts as a line driver. This is the Philips NE/SE592 video amplifier [9]. It is operated in the bandpass mode, by connecting a 910 Ω resistor, 4.7 μH inductor and 0.47 μF capacitor across the gain select pins, G_{1A} and G_{1B}.

Top hat functions were input into the video amplifier arrangement in order to observe its effects on a step input (theta function). The response to a step is illustrated in figure 15.

The response can be regarded as comprising of an exponential growth coupled with an exponential decay of time constants found experimentally to be approximately 0.3 μs and 21.0 μs respectively. This approach is equivalent to considering the video amplifier as performing differentiation followed by integration as in simple RC circuits. Thus, to calculate the effects of the video amplifier on the pulses, the pulses were regarded as being comprised of a series of steps (several thousand in fact). Each of which would generate a response as in figure 15 on passage through NE/SE592. A FORTRAN program was devised to sum these responses, for all the steps, with the appropriate start times. The gain provided by the video amplifier was also taken empirically by comparing the output amplitude to that of the input step. Figure 16 shows the calculated pulse on emergence from the video amplifier, taking figure 6 (a clever end hit) as the input pulse.

5.2 The shaper and the digitizer

After leaving the video amplifier the pulses from the anode wire enter the shaper circuit as shown in figure 17 and then finally the digitizing board, see figure 18.

The effects of the shaper circuit and the circuitry between exit from the shaper and entry into the digitizer chip, at pin 17 on figure 18, were again found by passing top hat functions, of varying widths, through the circuit. As in the case of the video amplifier the effects could be regarded with sufficient accuracy as equivalent to those produced by passing the pulses through a simple RC differentiator and integrator. The time constants for the growth and decay being 0.08 μs and 12.0 μs respectively, in this instance. Thus, the pulse on entry to the digitizer is illustrated in figure 19, as calculated by breaking the pulse of figure 16 into steps and summing responses as discussed in the preceeding subsection.

The pulse generated by the simulation compares favourably with the typical pulse at this stage, found by fitting curves to digitized raw data [10]. The simulation was utilized to generate a series of clever and dumb end pulses for various values of z along the wire, see figure 20. The clever end pulses decrease in height and increase in width as the location of the avalanche is moved away from the clever end. The midway hit at $z = 5\ m$ produces identical pulses for both ends illustrating the symmetry of the system. This symmetry is also bourne out in comparing the 0 m and 10 m hits.

Once the pulses enter chip TS8328, at pin 17, they become digitized and hence exist in a form that will not be altered by subsequent electronics. The digitizer is a 64-channel 12.5 MHz FADC (flash analogue to digital converter) FASTBUS and as such provides a digitization every 80 ns [11]. The process of digitization is easily simulated by a computer program, that samples the amplitude of the waveform at the required intervals.

6 Future Prospects

It is thus possible to generate pulses at particular values of z in the digitized form similar to that available from events at CERN. Hence, a test of the effectiveness of different algorithms may be made by comparing the values of z obtained using them to that input into the simulation.

Presently at CERN, the charge from a signal is taken to be the sum of all the positive going bins. Considering the shape modifications a pulse undergoes, as discussed in the body of this paper, this method can be regarded as an over simplification. A typical pulse will have ~ 4 positive bins and ignoring the large number of negative bins means much information about the pulses is neglected. It may be possible to deduce the most appropriate algorithm to be used by weighting the contents of the bins before combination in such a way to produce the value of z entered into the program. Also, a better understanding of the shape of the pulse signals, implies the possibility of an improved double hit resolution for the muon chambers.

7 Conclusion

The analysis of the movement of positive ions within a muon barrel chamber coupled with the solution of the equivalent circuit of figure 5 allowed a pulse simulation program to be constructed. The simulation generates the pulses from both ends of the anode wire and these compare well with empirical observations of pulses at various stages throughout the system. The simulation allows the z coordinate of the avalanche to be selected and the variation of clever and dumb end signals with z coordinate has been studied.

8 Acknowledgements

I would like to thank R. Barlow, the provider of essential motivation during the production of this work. D. Mercer and A. A. Macbeth deserve much acknowledgement for sharing their vast electronics expertise. Also, thanks must go to I. Duerdoth for many helpful comments on the manuscript, to J. Allison, who provided Figure 4 and A. O'Dowd for additional help on a variety of topics.

References

[1] J. Allison *et al. The OPAL muon barrel drift chambers*, in preparation.

[2] I. P. Duerdoth. Proc. The Position Sensitive Detectors Conf. , London, 1990., J. Allison et al., Manchester Preprint MAN/HEP/91/01

[3] J.Allison *et al. Diamond Shaped Cathode Pads for the Longitudinal Coordinate from a Drift Chamber.* Nucl. Instr. and Meth. A236 284, 1985.

[4] V. Radeka and P. Rehak, IEEE Trans. Nucl. Sci. NS-26 (1979) 225

[5] I. P. Duerdoth Manchester Preprint MAN/HEP/91/02, 1991

[6] *Review of Particle Properties.* Phys.Lett. B204 (1988) 61

[7] F. Sauli *Principles and Operation of Multiwire Proportional and Drift Chambers.* CERN Report 77-09 (1977)

[8] The NAG Fortran Library Manual - Mark 13, Vol. 2, Ch. D02.

[9] Philips Integrated Circuits Data handbook IC11, 1988.

[10] S. Pawley. Advanced Diploma in Science, University of Manchester, 1989.

[11] TPD FASTBUS Modules Type F6821, Invitation to Tender I-1410/EF, CERN-EP-EL, 86.01.28.

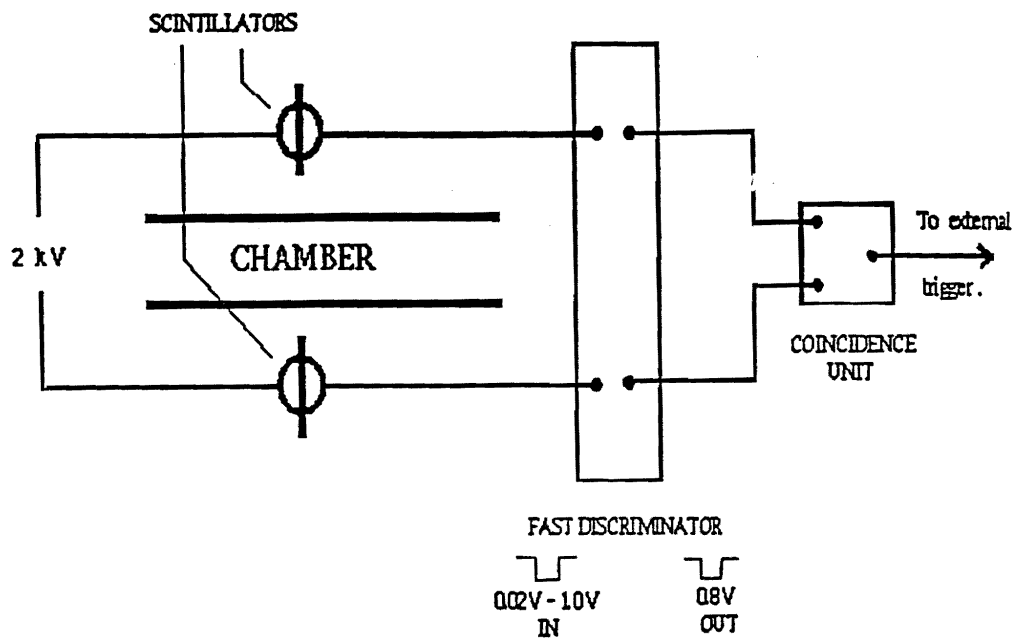

Figure 1: Chamber set up to observe cosmic rays.

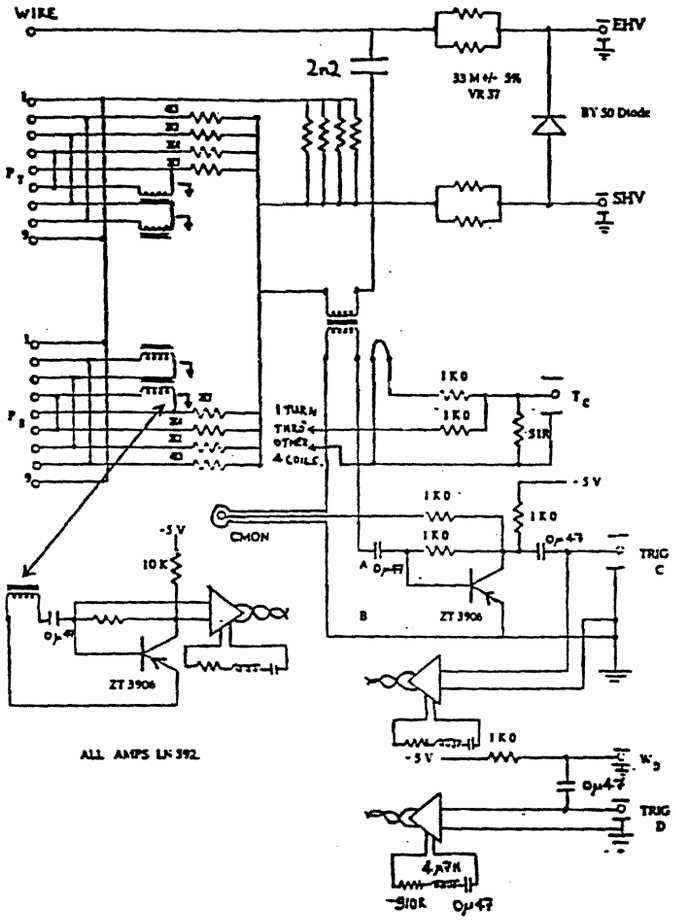

Figure 2: The preamplifier board C.

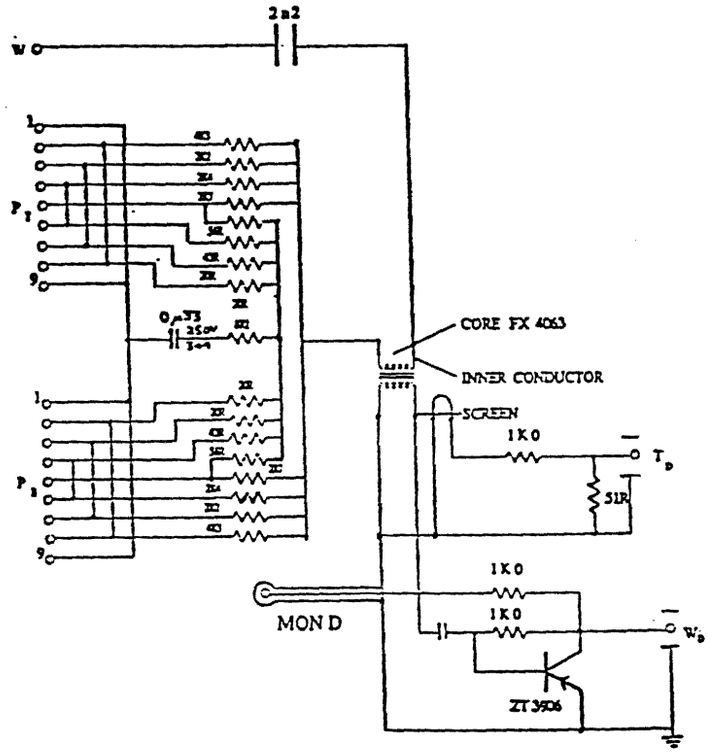

Figure 3: The preamplifier board D.

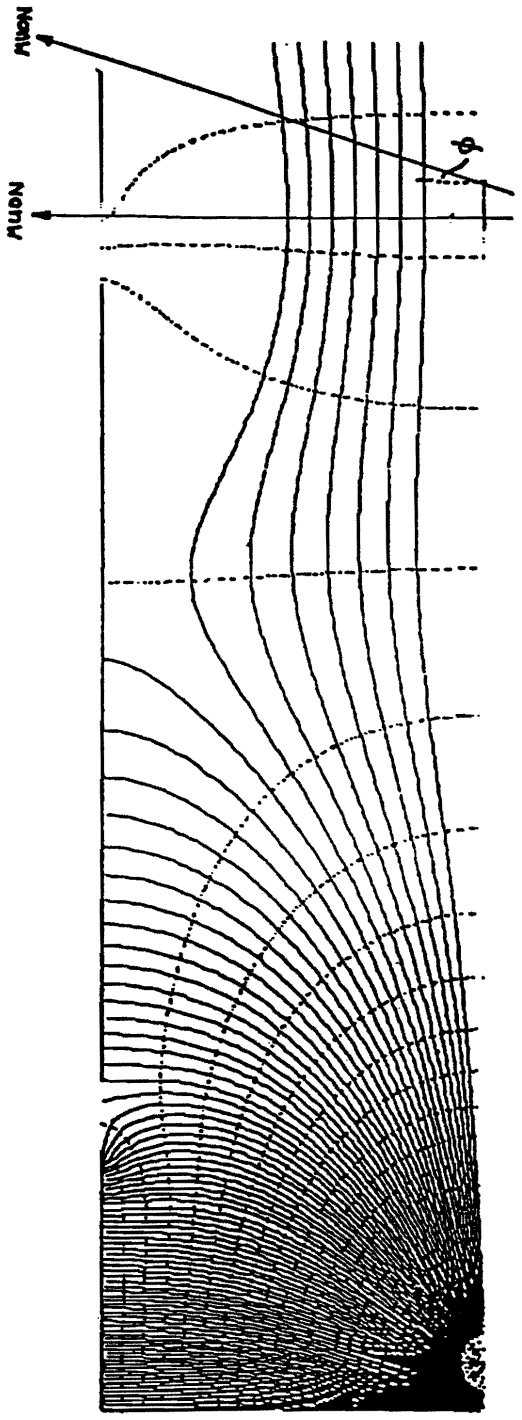

Figure4: The field within an OPAL drift chamber.

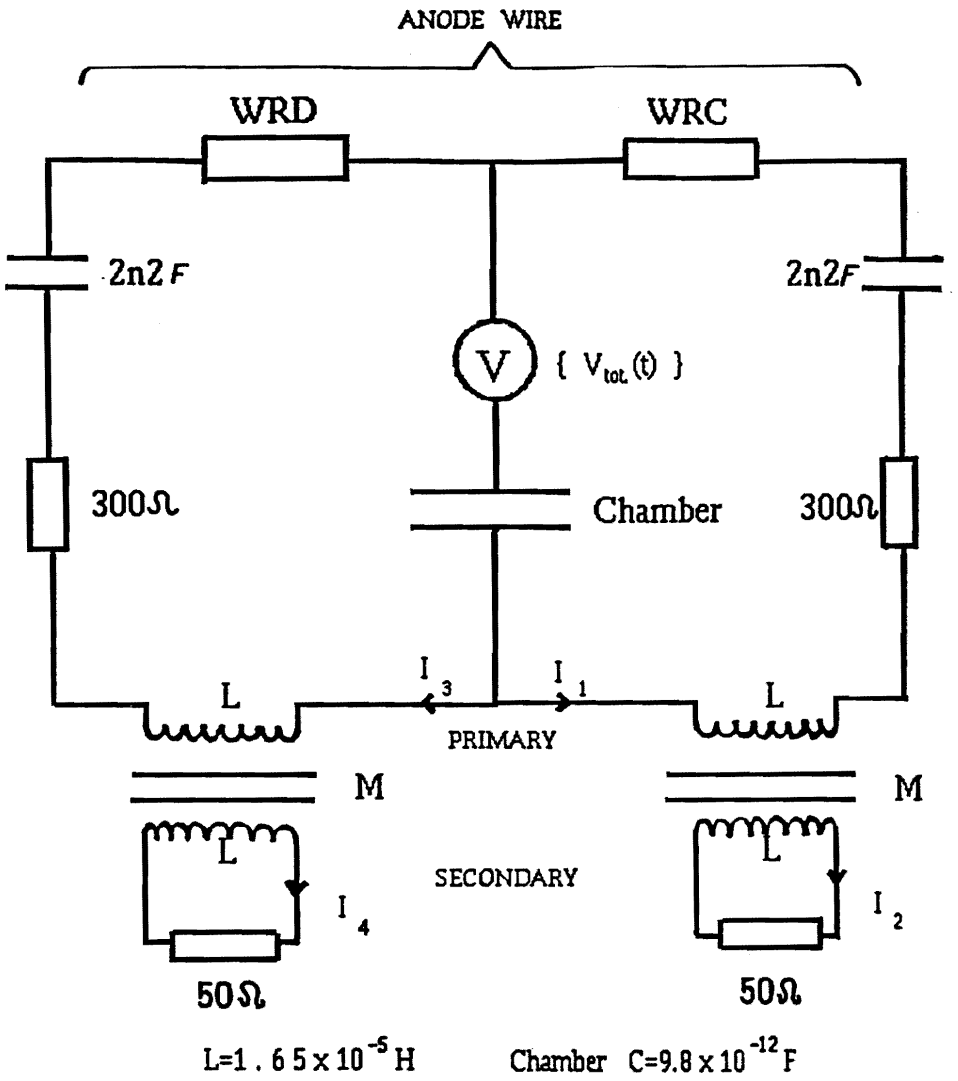

Figure 5: The chamber circuit to the transformers on the preamplifier boards.

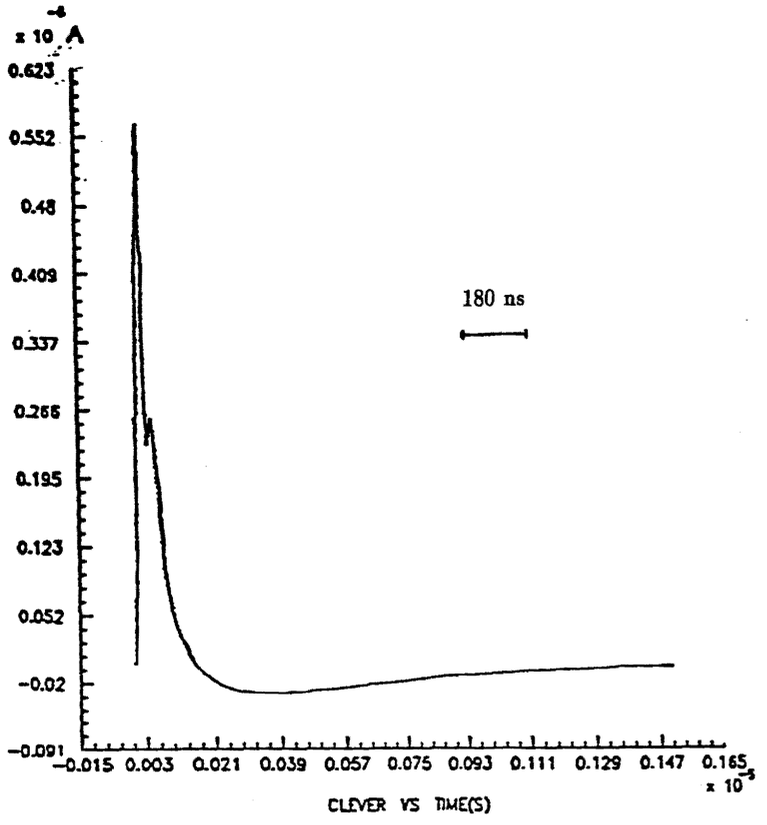

Figure 6 : Pulse simulation at normal incidence near to the clever end.

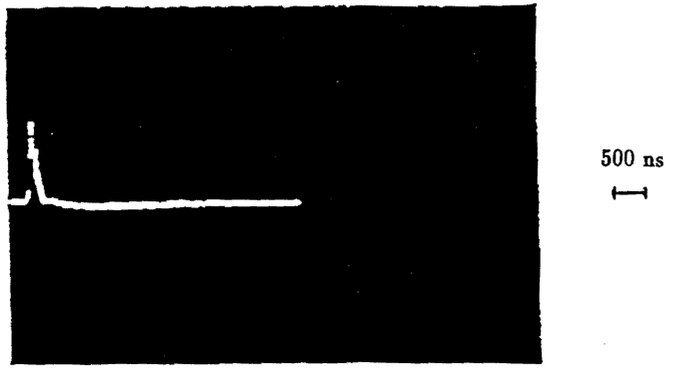

Figure 7 : Pulse observed at MON C normal incidence near to the clever end.

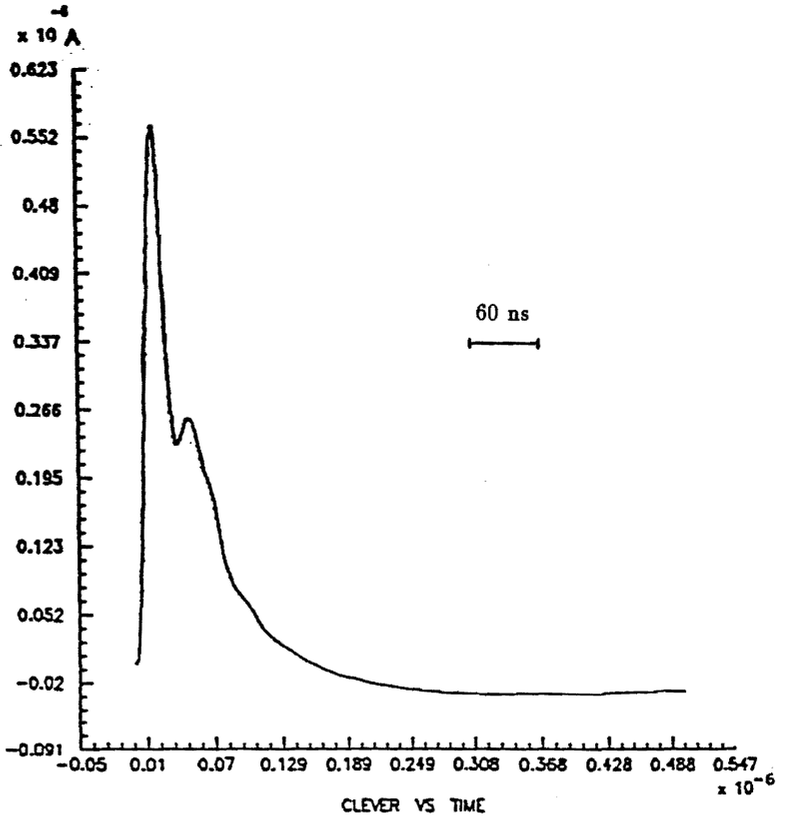

Figure 8 : Pulse simulation at normal incidence to the clever end, $0 < t < 500ns$.

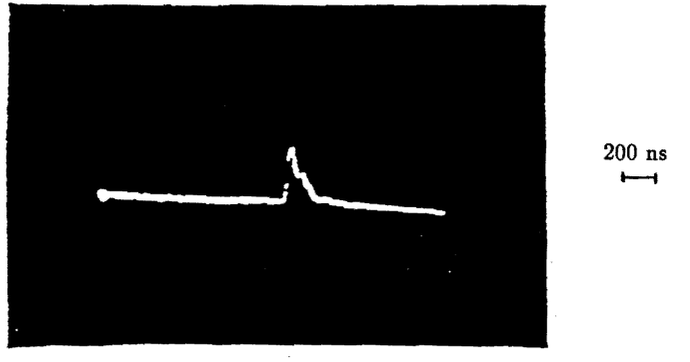

Figure 9 : Pulse observed at MON C with a time base of 0.2 $\mu s div^{-1}$.

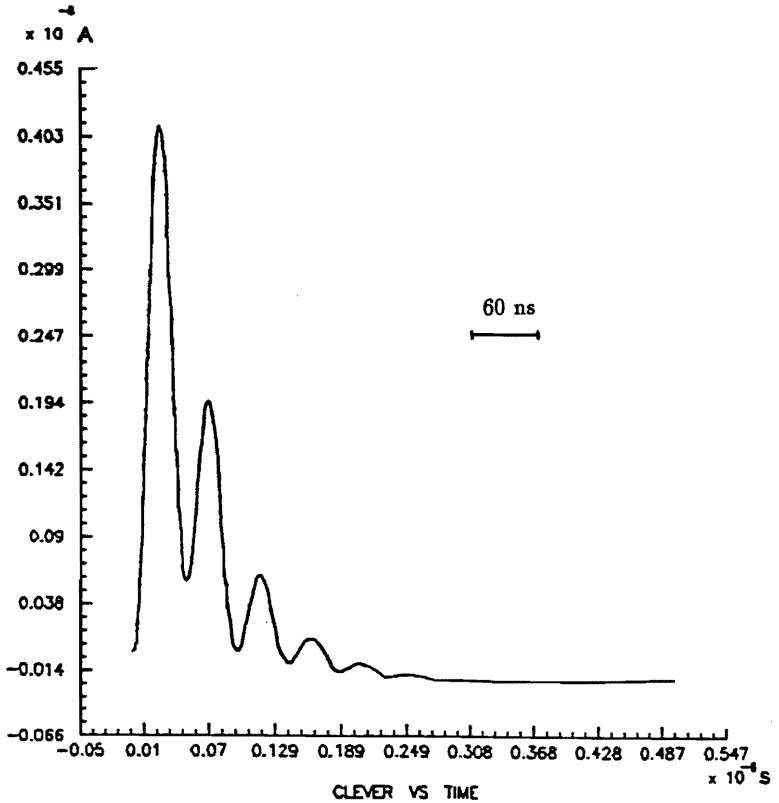

Figure 10: Pulse simulation at normal incidence near to the clever end with mutual linkage of 60 %.

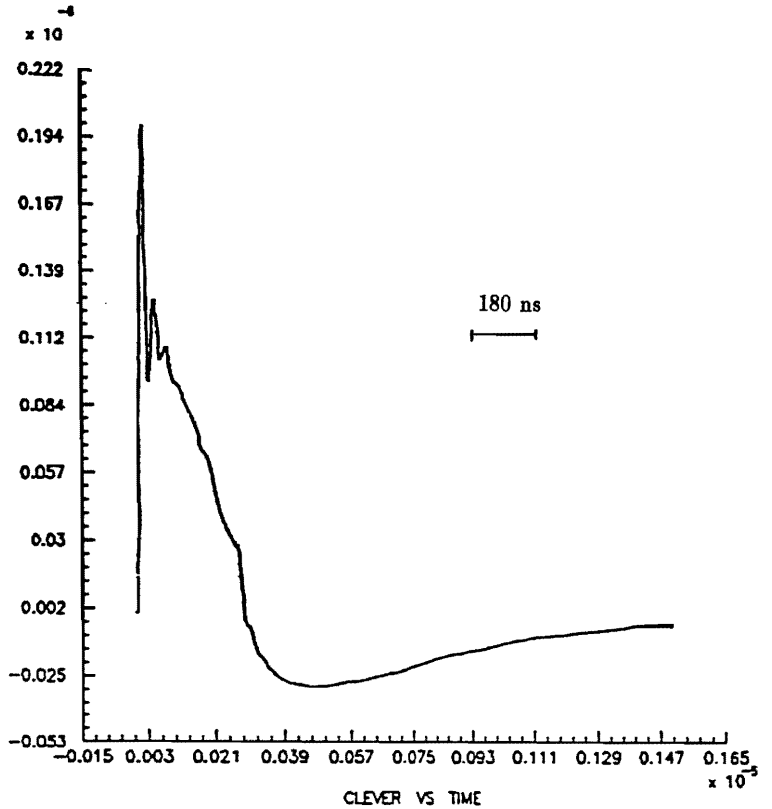

Figure 11: Pulse simulation at an angle $\phi = 45°$.

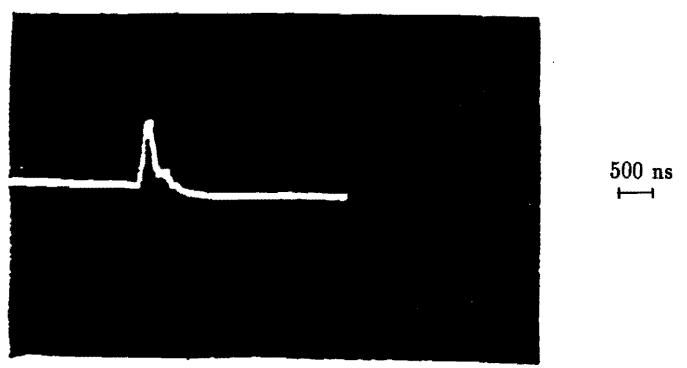

Figure 12: Pulse observed at MON C at an angle $\phi = 45°$.

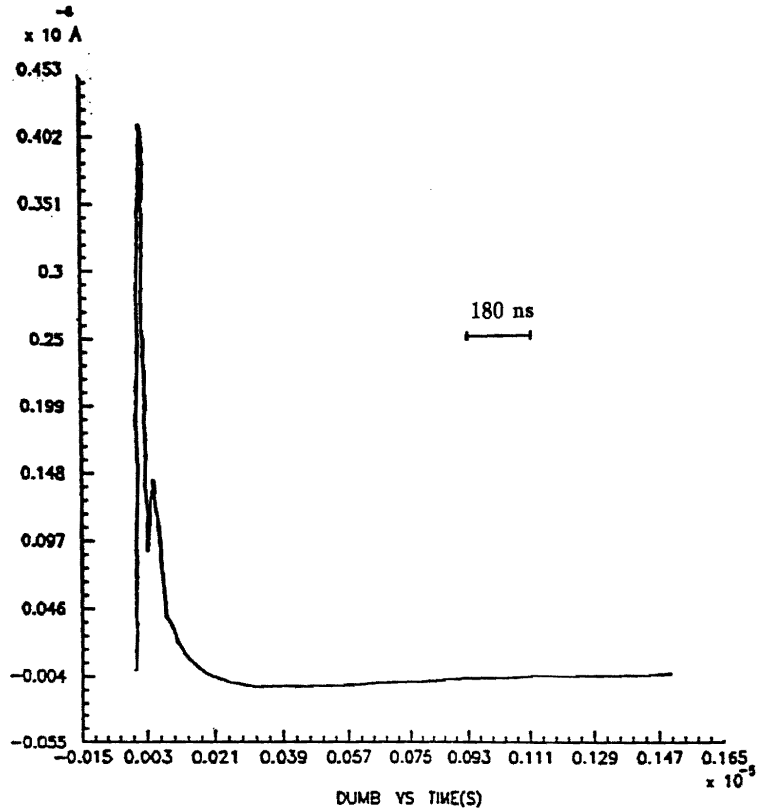

Figure 13: Pulse simulation at the dumb end for a clever end incident particle.

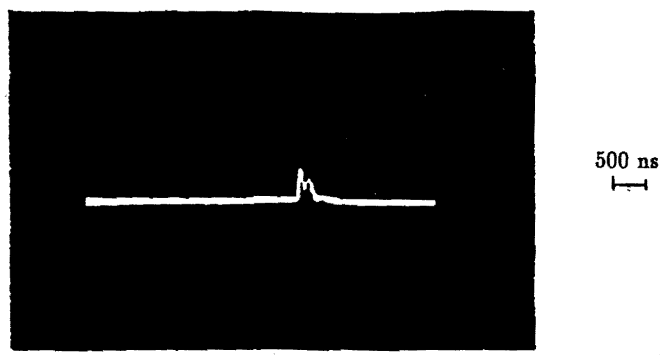

Figure 14: Pulse observed at MON D.

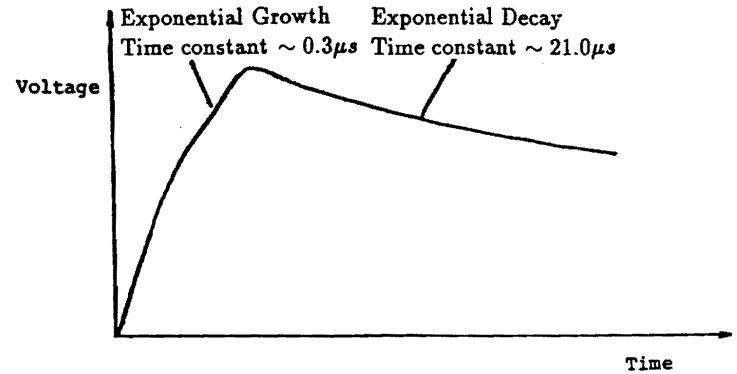

Figure 15: The video amplifier response to a step.

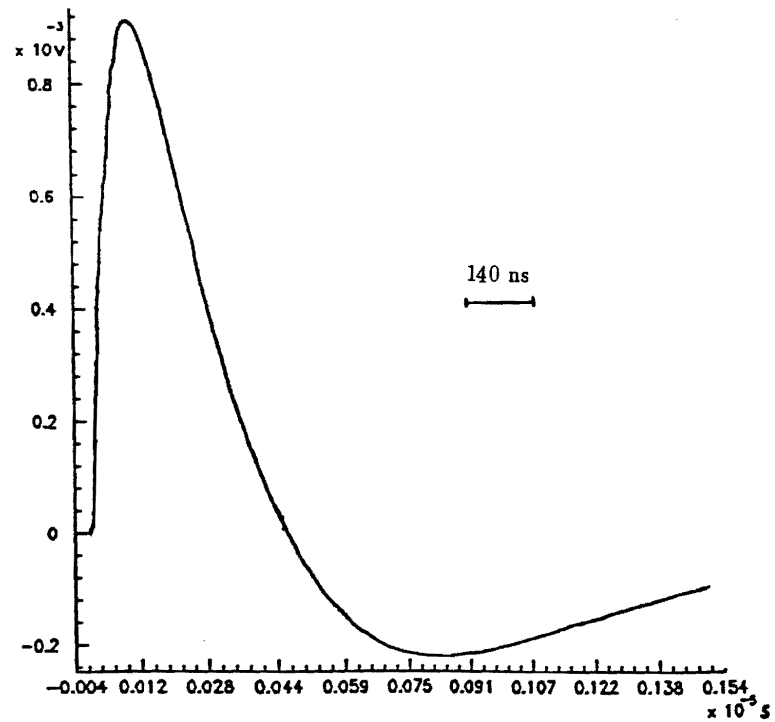

Figure 16: Clever end, incident particle, pulse after the video amplifier. The video amplifier widens the pulse and gives the large overshoot. The amplitude of the overshoot is ~ 20% of that of the peak.

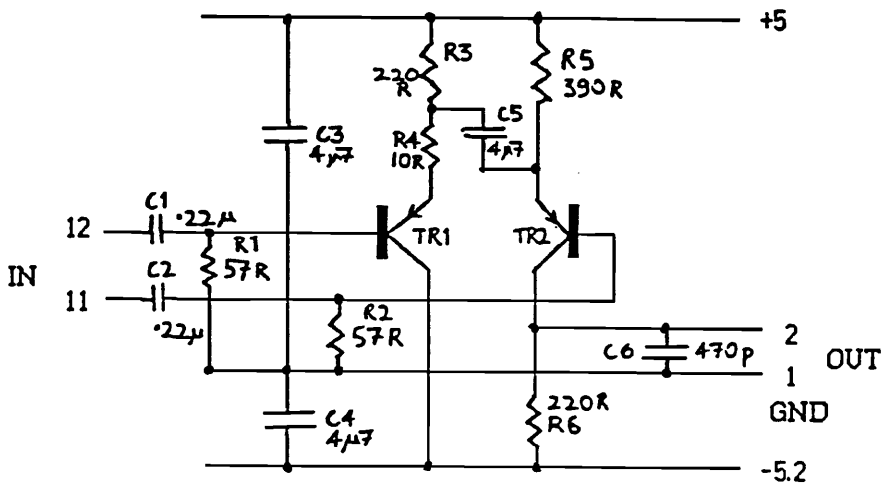

Figure 17: The shaper circuit.

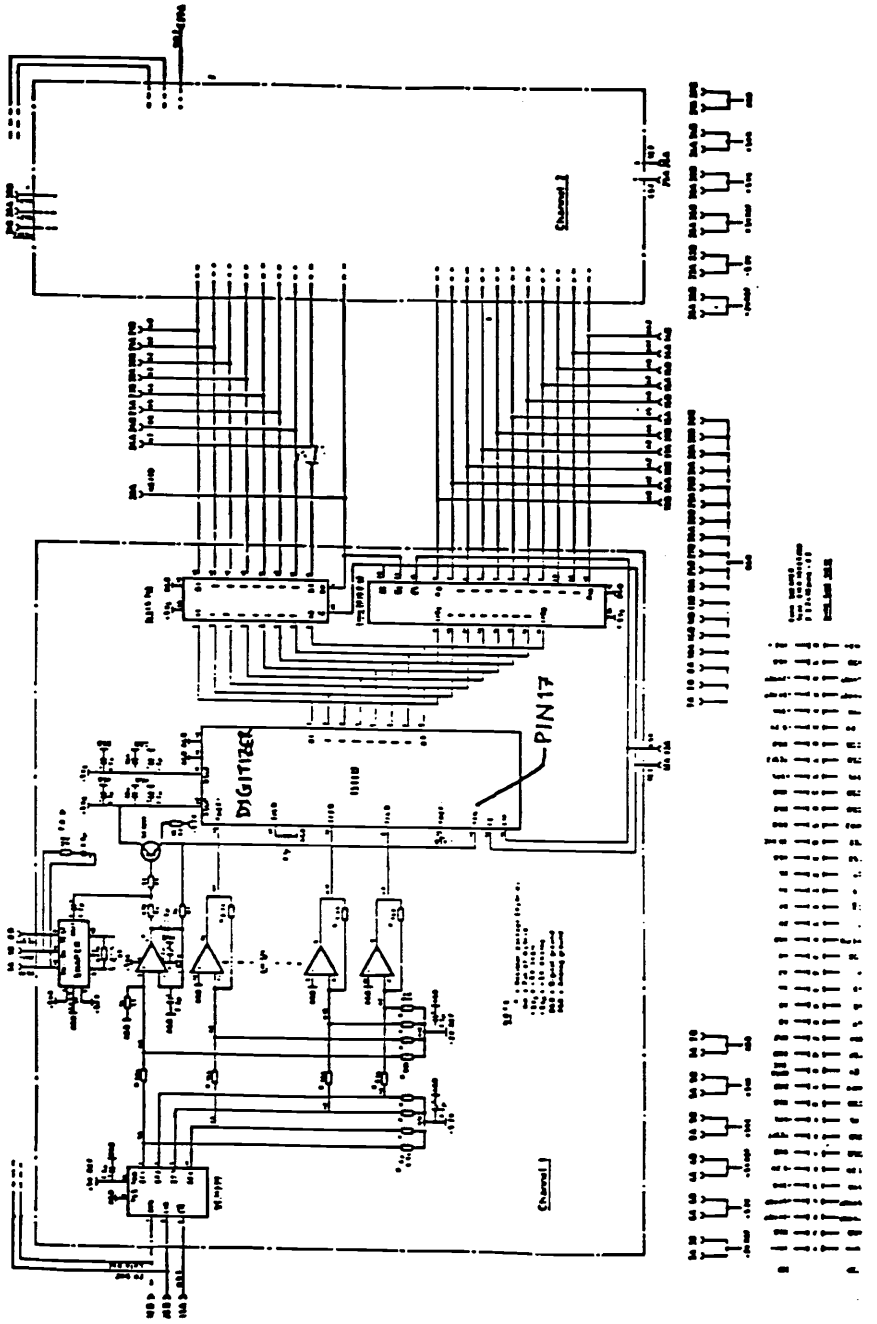

Figure 18: The daughter board of the FADC.

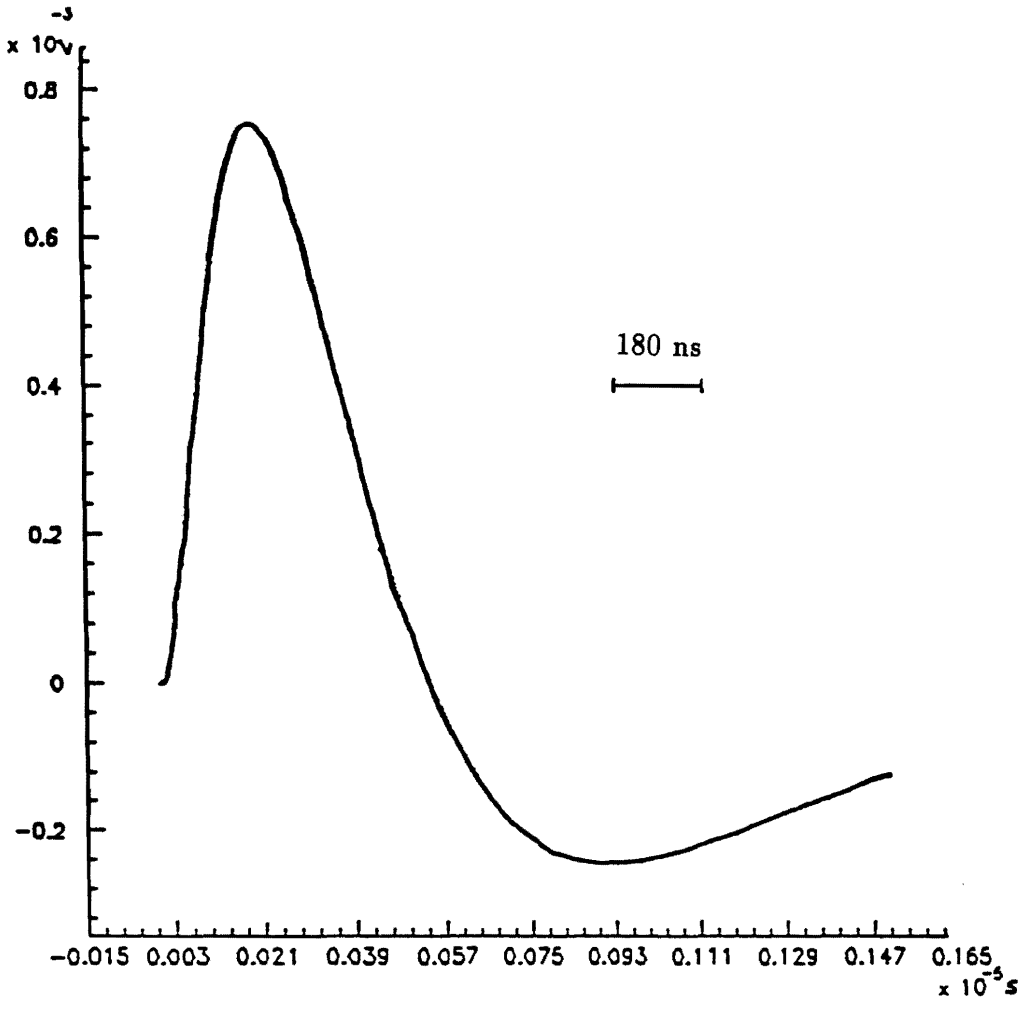

Figure 19: Clever end hit (z = 0 m) pulse on entry to the digitizer as seen by the clever end.

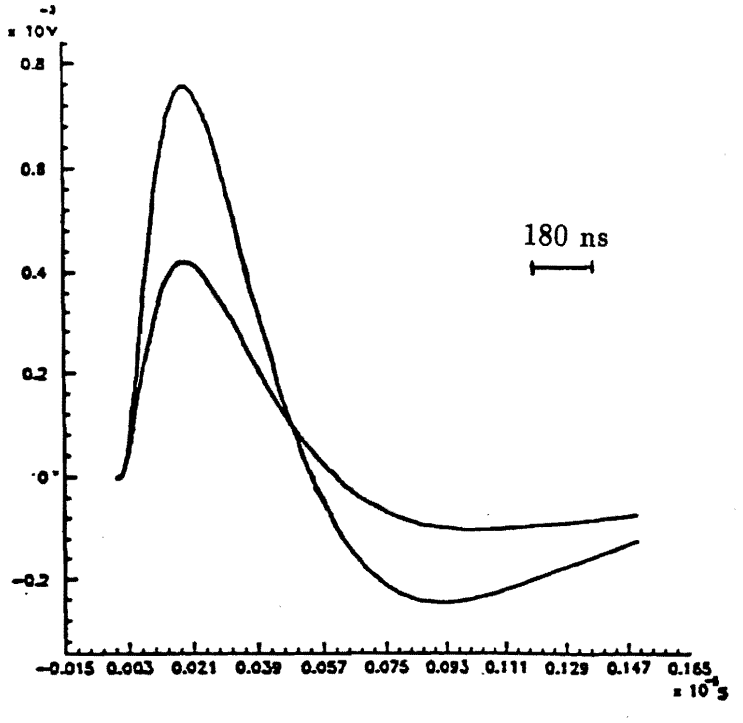

Figure 20a): Clever and dumb signals z=0m
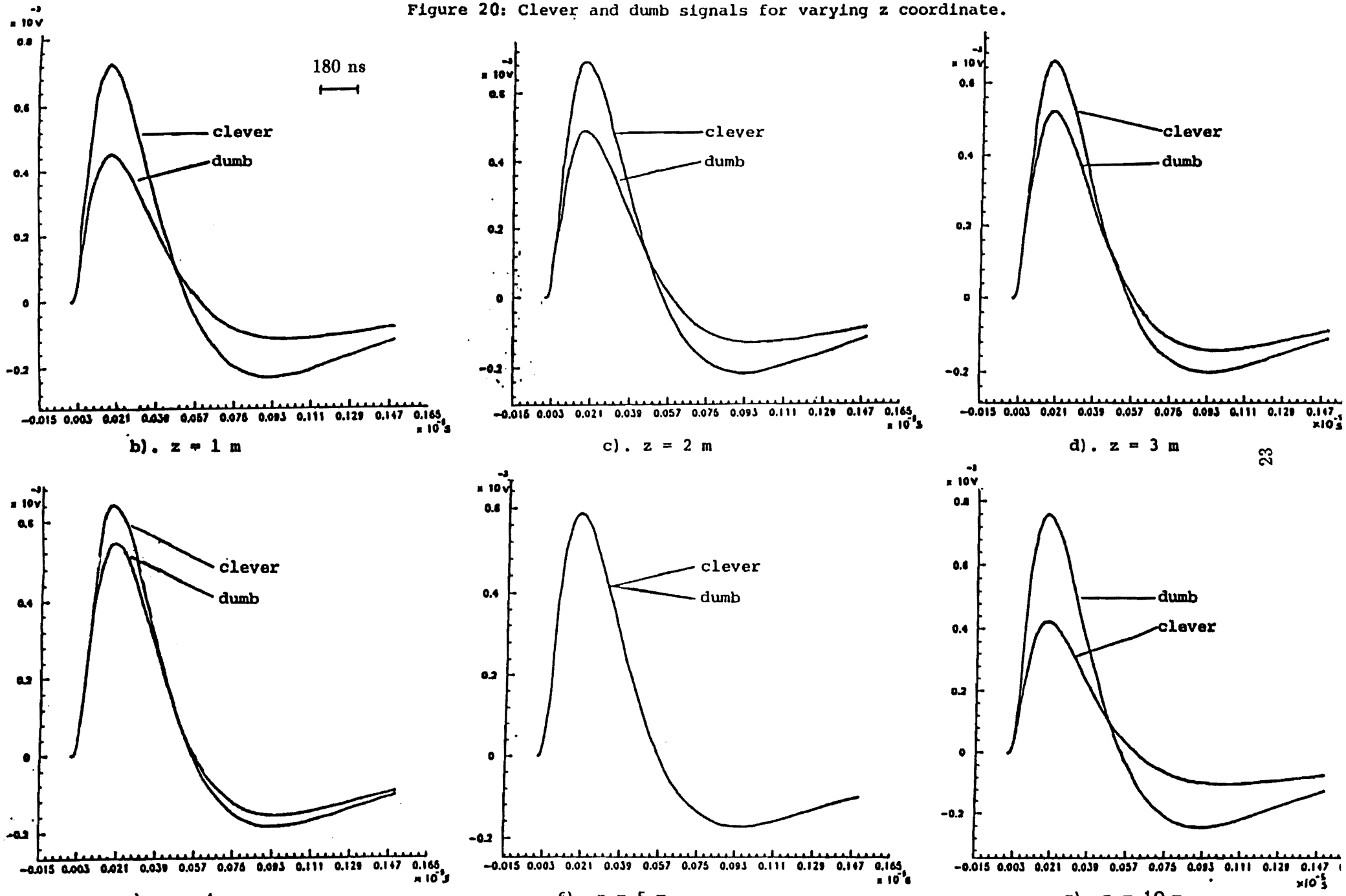
Figure 20: Clever and dumb signals for varying z coordinate.